

Kinetics, Statistics, and Energetics of Lipid Membrane Electroporation Studied by Molecular Dynamics Simulations

Rainer A. Böckmann,* Bert L. de Groot,[†] Sergej Kakorin,[‡] Eberhard Neumann,[‡] and Helmut Grubmüller[§]

*Theoretical & Computational Membrane Biology, Center for Bioinformatics, Saarland University, Saarbrücken, Germany; [†]Computational Biomolecular Dynamics Group, Max-Planck-Institute for Biophysical Chemistry, Göttingen, Germany; [‡]Physical Chemistry III (Bio-PC), Department for Chemistry, University of Bielefeld, Bielefeld, Germany; and [§]Theoretical and Computational Biophysics Department, Max-Planck-Institute for Biophysical Chemistry, Göttingen, Germany

ABSTRACT Membrane electroporation is the method to directly transfer bioactive substances such as drugs and genes into living cells, as well as preceding electrofusion. Although much information on the microscopic mechanism has been obtained both from experiment and simulation, the existence and nature of possible intermediates is still unclear. To elucidate intermediates of electropore formation by direct comparison with measured prepore formation kinetics, we have carried out 49 atomistic electroporation simulations on a palmitoyl-oleoyl-phosphatidylcholine bilayer for electric field strengths between 0.04 and 0.7 V/nm. A statistical theory is developed to facilitate direct comparison of experimental (macroscopic) prepore formation kinetics with the (single event) preparation times derived from the simulations, which also allows us to extract an effective number of lipids involved in each pore formation event. A linear dependency of the activation energy for prepore formation on the applied field is seen, with quantitative agreement between experiment and simulation. The distribution of preparation times suggests a four-state pore formation model. The model involves a first intermediate characterized by a differential tilt of the polar lipid headgroups on both leaflets, and a second intermediate (prepore), where a polar chain across the bilayer is formed by 3–4 lipid headgroups and several water molecules, thereby providing a microscopic explanation for the polarizable volume derived previously from the measured kinetics. An average pore radius of 0.47 ± 0.15 nm is seen, in favorable agreement with conductance measurements and electrooptical experiments of lipid vesicles.

INTRODUCTION

Membrane electroporation (MEP) is nowadays an established technique to render cell membranes porous and permeable by applying electric pulses to cells in suspension (1), adherent cells, and tissue. Historically, the structural concept of MEP has been derived from functional changes such as cell death (2), the nondestructive electro-release of intracellular components from isolated organelles (3), and the functional direct electro-uptake of naked gene DNA into mouse lymphoma cells (1). MEP is widely used for the efficient direct electrotransfer of all kinds of bioactive substances, in particular drugs and genes, not only in cell biology and biotechnology but also in the new medical disciplines of electrochemotherapy (4,5) and electrogenotherapy (6) used, e.g., for vaccination (7,8) or in RNA transfection (9,10). Other electroporative phenomena such as electrofusion of cells (11,12) or electroinsertion of xenoproteins by non-permeabilizing electroporation pulses at low voltages (13) are intrinsically coupled to the structural changes of MEP.

The physical chemical data of cells and lipid model systems clearly indicates that the electric field effects involved in MEP primarily reflect structural changes in the lipid part of the biomembranes (14). Remarkably, a direct field effect on the ionic-polar headgroups of the membrane lipids has been suggested for the field-induced rearrangements of lipid

molecules leading to localized hydrophilic pores from the very beginning (1). Interestingly, the conductance changes of electroporated erythrocyte ghosts have been interpreted in terms of nanometer-sized aqueous pores, quantified by numerical values of pore radius and number of pores (15). Conductive pores are also indicated in artificial lipid bilayer systems, black lipid membranes, by the fluctuations of single-conductance events (16,17). Both the time interval (delay time) leading to the inevitable rupture of the black lipid membranes and the time interval up to the onset of recorded single current events have been documented as a function of field strength (16,17). The dependence of the lag times on the transmembrane voltage has been used to distinguish between different pore formation theories (18). Besides electric pore formation, electric pulses lead to field-induced vesicle shape deformations (19). Deformations toward ellipsoids occur at constant volume if the pulse duration is too short to permit measurable release of intracellular salt ions. The shape change is concomitant with an increase in the membrane surface area, due to the entering of water to form pores, thereby increasing the refractive index of the membrane. The concomitant conductance increase and the (high-field) release of salt ions are clearcut indicators for conductive aqueous pores (electropores). A variety of other transport phenomena in unilamellar vesicles have also been interpreted in terms of electropores (20).

Electrothermodynamically, the structural membrane changes accompanying MEP have been quantitatively characterized

Submitted January 14, 2008, and accepted for publication March 31, 2008.

Address reprint requests to Rainer A. Böckmann, E-mail: rainer@bioinformatik.uni-saarland.de.

Editor: Peter C. Jordan.

© 2008 by the Biophysical Society
0006-3495/08/08/1837/14 \$2.00

doi: 10.1529/biophysj.108.129437

in terms of the mean polarization volume v_p ; assuming cylindrical pores where $v_p = \pi \cdot r_p^2 \cdot d_m$ and $d_m = 5$ nm is the membrane thickness, a mean pore radius r_p can be determined. In lipid vesicles as well as in cell membranes, various types of electropores occur: short-lived small pores ($r_p \approx 0.4$ nm) and long-lived larger pores ($r_p \geq 1$ nm). In a recent molecular-dynamics simulation study of a bilayer consisting of >2300 lipids in an external electric field of $E = 0.5$ V/nm, pores were found to grow up to 10 nm in diameter within the accessible simulation time of <4 ns (21). After formation of a single-file water defect, pores grew quickly in size, without an observable intermediate and without an observed limit in pore size (21). The field-dependence of pore formation times was not studied. Recently, a strong alignment of lipid head-groups within the pore region was reported (22). In another study, time-dependent electric fields mimicking nanosecond pulses used in experiments were employed (23,24); however, compared to the former study by Tieleman (21), no significant influence of the modified pulse shape on pore formation was reported. Gurtovenko and Vattulainen (25–27) subsequently showed transient pore formation in phospholipid bilayers induced solely through charge imbalance across the bilayer. A stabilizing effect of proteins (gramicidin) on phospholipid bilayers was found both from the measured increased voltage-threshold for electroporation for gramicidin-doped bilayers with respect to pure phospholipid bilayers (28) and in simulations by the decreased typical pore formation times for a protein-free membrane with respect to a gramicidin-lipid system (29). Phosphatidylserine (PS) translocation in asymmetric bilayers has been shown to occur after electropore formation (30).

Finally, high external voltages were hypothesized to induce nanoscale membrane fragmentation, possibly of importance for electrofusion of membranes (31).

A characteristic feature of MEP is the occurrence of field-dependent temporal lag phases, both in the conductance relaxations of spherical erythrocyte ghosts (15) and lipid vesicles and in the metastable planar lipid bilayers (16). The lag-phases clearly precede the onset of the actual pore formations. Due to the tension exerted by the lipid torus, pore formation in the metastable bilayers leads, however, to rupture of the bilayer. The dependence of this lag time on the transmembrane voltage has been used to distinguish between different pore formation theories (18). Electrooptical and conductometrical data of salt-filled vesicles in isoosmolar sucrose solution yield a delayed exponential increase in the fraction of hydrophilic pores associated with a surface area increase due to water entrance as a function of time t (32). The delay time constant decreases with increasing field strength and requires two intermediate preparation steps.

Despite these achievements, several questions remain unanswered (see, e.g., (33) for a review). For example, an intermediate on the way to hydrophilic pores has been proposed and tentatively been assigned a hydrophobic pore (see Fig. 1) on the basis of kinetic measurements (16,34). Also,

conductance measurements on planar lipid bilayers showed the existence of a nonconductive prepore state (17). However, in none of the simulations such a hydrophobic pore has been observed. Accordingly, the structural features of such an intermediate are still unknown. In particular, it is still unclear how transient exposure of larger hydrophobic lipid tail surface areas can be avoided before the thermodynamically much more plausible inverted hydrophilic pore is formed—which otherwise would imply a free energy barrier that is much too large to account for the observed kinetics with time constants of $\tau_p = 0.5 \dots 5 \mu\text{s}$ (32).

A second line of questions concerns the primary event that ultimately initiates pore formation, as well as triggering events. Sheer fluctuations of membrane defects have been suggested as one possible trigger, but the specific mechanism remains unclear. Atomic scale simulations (21,23–25,29,35,36) indicated a water defect in the membrane as the first step of pore formation. This primary event will determine the electric field dependency of electropore formation.

A third issue is that, to our very best knowledge, no attempt has been made so far to quantitatively relate the pore formation times observed in simulations to measured pore formation kinetics, such that up to now the simulations have not been rigorously validated against experiment. As we will detail below, such a comparison is highly nontrivial and complicated for two reasons. First, the usual implementation of external electric fields in molecular dynamics force fields using particle mesh Ewald (PME) and periodic boundary conditions allow—contrary to naive expectation—no direct control of the electric field strength within the simulation system. Rather, the external electric field strength effectively applied depends on the polarizability of the system and, hence, varies with position and time during the simulation. This effect is here accounted for by explicit determination of the local electric field from the simulations. Second, the experimental observable—the pore formation kinetics, characterized by time constants τ —is conceptually different from the mean pore formation time $\langle t^* \rangle$ as derived from the simulations. In particular, the ensemble average τ is independent of the size of the lipid patch considered; in contrast, the probability of observing a first pore in a small simulation patch increases with patch size and, hence, $\langle t^* \rangle$ decreases. A framework therefore needs to be formulated which properly relates these two quantities to each other.

In summary, the details of the molecular mechanism of MEP are still controversially discussed. The details of the action of the electric field on the lipid molecules as well as on the positional dynamics of the lipids within the bilayer are not yet sufficiently characterized at the atomic level.

Here, we present an atomistic model for the processes leading finally to the formation of aqueous pores. Our approach is based on extensive molecular dynamics simulations of phospholipid bilayers in electric fields of low (0.04 V/nm) to high (0.7 V/nm) strengths, totaling $\sim 1 \mu\text{s}$. We will compare the obtained distribution of microscopic lag times pre-

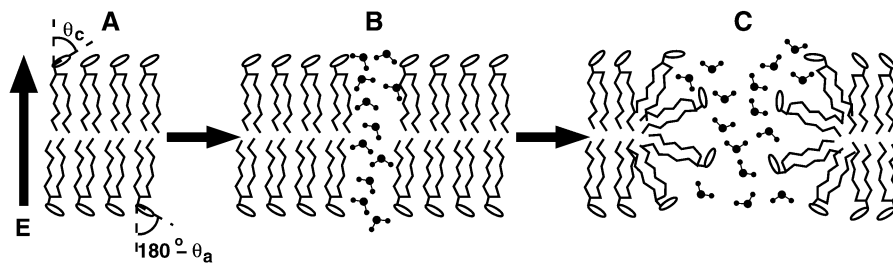


FIGURE 1 Sketch of a cross section through a lipid bilayer: ideal, at $E = 0$ V/m (A), a small hydrophobic pore intermediate (B) during electropore formation, and the stable hydrophilic pore (C), where the pore wall contains tilted lipids with the dipolar headgroups aligned parallel to the external field vector \mathbf{E}_{ext} . θ is the average angle between the (lipid) molecular dipole moment (μ) and \mathbf{E}_{ext} . On the cathodic side, $\theta_c = 70 \pm 2^\circ$, and on the anodic side, $\theta_a = 110 \pm 2^\circ$.

ceding pore formation with experimental lag times obtained from the kinetics of an ensemble of unilamellar vesicles in suspension. The obtained pore formation times will then be analyzed within a coherent kinetic framework. Furthermore, interactions between the lipids and adjacent water layers are revisited and analyzed in detail. The equilibrium size of an electropore is studied for an intermediate electric field. A comprehensive molecular picture of the molecular mechanism of MEP is obtained, consistent with available experimental data.

METHODS

Molecular dynamics simulations

Bilayer patches composed of 128 (system A) and 512 (system B) palmitoyl-oleoyl-phosphatidylcholine (POPC) lipids surrounded by explicit water were studied. The small system was used for studying the pore formation kinetics, requiring many simulations at varying field strengths. The four times larger system was used for the study of a stable electropore. A preequilibrated POPC bilayer (37) was used as a start structure. Force field parameters for the lipids were taken from Berger et al. (38), and the parameters for the unsaturated carbons from the GROMOS87 force field. All simulations were performed in a periodic box filled with >5100 SPC (39) water molecules corresponding to a hydration level of ~ 37 waters/lipid, yielding a total system size of $>21,000$ (88,000) atoms (Fig. 2). Ions were only considered within simulation system B, because it was shown that their influence on the electrostatic field across the membrane is negligible (37) and because (equilibrated) ions showed little influence on the electropore formation process in MD simulations of a DOPC bilayer (21). Test simulations (data not shown) of the investigated POPC bilayer did not reveal any significant participation of ions in the pore formation process, too.

The relatively small size of system A enabled us to carry out 48 simulations with different external electric field strengths ranging from 0.7 V/nm down to 0.1 V/nm (see Table 1). Additionally, to investigate stable hydrophilic pores in the nanometer range at close-to physiological conditions, the larger system B (see Fig. 2) was simulated at 100 mM $\text{Na}^+ \text{Cl}^-$ concentration until a prepore was formed (after 900 ps at an electric field of 0.5 V/nm) and subsequently at a decreased field strength of 0.04 V/nm for 50 ns (for details, see below).

Field-induced structural changes of the bilayer were obtained by comparison with a previously described 200-ns simulation of a POPC bilayer with 128 POPC lipids without external electric field (37,40). The total simulation time of the described simulations was 0.88 μs for the 128 POPC system and 40 ns for the 512 POPC system.

All MD simulations were carried out using the GROMACS simulation suite (41,42). Application of the LINCS (43) and SETTLE (44) methods allowed for an integration step size of 2 fs. Electrostatic interactions were calculated with PME (45) with tin-foil boundary conditions (46,47). The temperature was coupled to an external temperature bath (48) at 300 K with a coupling constant of $\tau_T = 0.1$ ps separately for the lipids and the solvent. The

pressure was kept constant by weak semiisotropic coupling to a pressure bath (48) with $\tau_p = 1$ ps (separately for the lateral and normal directions).

In the MD simulations, an external electric field \mathbf{E}_{ext} was applied parallel to the membrane normal z , i.e., perpendicular to the bilayer surface. This was done by including additional forces $\mathbf{F}_i = q_i \mathbf{E}_{\text{ext}}$ acting on all charged atoms i within the simulation system. Accordingly, dipoles with the effective dipole moment \mathbf{m} are subjected to a torque $\mathbf{T} = \mathbf{m} \times \mathbf{E}_{\text{eff}}$, where \mathbf{E} is the effective field strength at the position of the dipole.

Lipid protrusions

Protrusions of individual lipids into or out of the bilayer were counted as follows. The monolayer surfaces were approximated by a Gaussian fit (width 0.88 nm) of the center of mass of the lipid headgroups of the respective layers to a grid with spacing 0.57 nm. Individual lipids were subsequently counted as protrusions if their headgroup center of mass deviates in direction of the bilayer normal by >0.6 nm from the neighboring grid positions. To avoid double-counting, lipids already identified as protrusions were not counted in subsequent timesteps until they have approached the grid to <0.2 nm.

Pore formation times

For each of the 48 simulations, prepore formation times were determined by visual inspection of snapshots taken from the simulations. A prepore was defined to be established if a closed water file connects both lipid leaflets.

Determination of the effective electric field in the simulations

The effective macroscopic electric field \mathbf{E} in our periodic boundary simulation setup depends on the choice of the (infinite) PME electrostatic boundary conditions and, therefore, needs careful consideration. In particular, it will not be identical to the applied field \mathbf{E}_{ext} . We note in this context that the total macroscopic electric field inside a pure water box is given by the sum of the external electric field \mathbf{E}_{ext} and the depolarization field \mathbf{E}_{dep} originating from the induced polarization of the medium:

$$\mathbf{E} = \mathbf{E}_{\text{ext}} + \mathbf{E}_{\text{dep}}. \quad (1)$$

As in previous simulations (21–24,26,30,36), tin-foil boundary conditions have been used in this study, which counteract surface charges induced by the dipoles within the simulation cell. As a result of this choice—and in harsh contrast to any experimental situation—the macroscopic electric field within a homogenic dielectricum such as pure water is enforced by the applied boundary conditions to equal the external field (49),

$$\mathbf{E} = \mathbf{E}_{\text{ext}}, \quad (2)$$

and, therefore, cannot be related to experiment in a comparably straightforward manner. For a homogeneous medium, comparison of the two equations allows us to calculate the external field effectively applied under these circumstances.

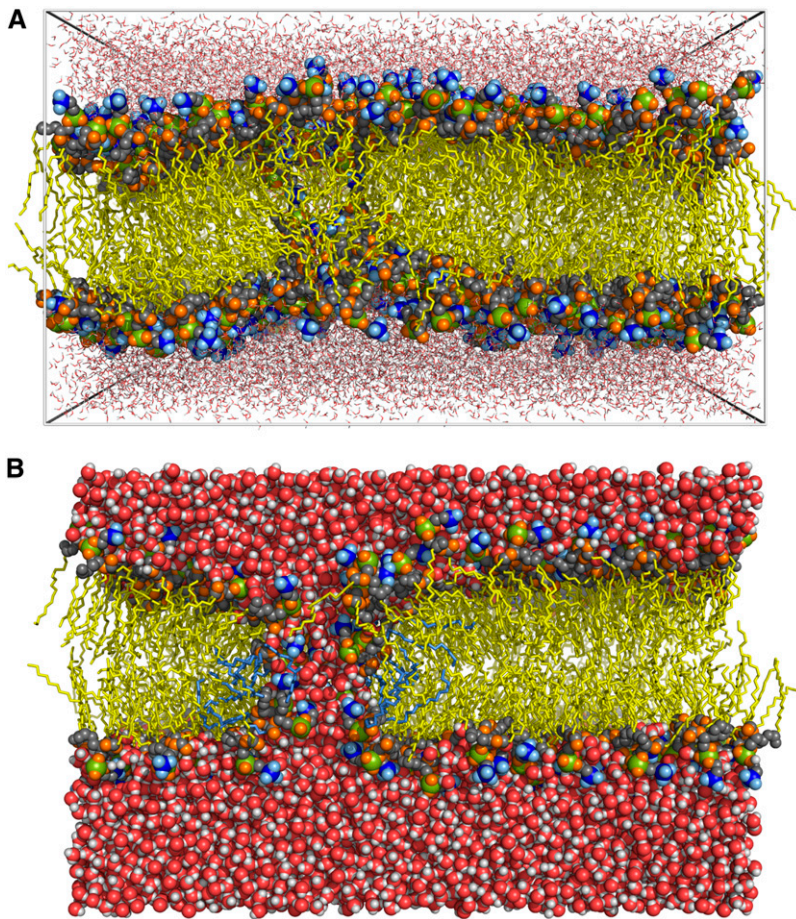


FIGURE 2 Simulation system with 512 POPC lipids after prepore formation (snapshot after 900 ps) at an electric field strength of $E = 0.5$ V/nm (A) and after 50 ns subsequent equilibration at a decreased field strength of $E = 0.04$ V/nm (B). Lipid tails are depicted as yellow sticks, the choline groups as blue spheres, the phosphorus atoms in green, lipid oxygen atoms in orange, and lipid head carbon atoms in gray. Water is shown in stick representation (A) and in space-filled representation (B), respectively. In panel B, a cut through the center of the pore is shown.

For the general case of an inhomogeneous dielectric, however, the polarization

$$\mathbf{P} = (\epsilon - \epsilon_\infty)\epsilon_0\mathbf{E} \quad (3)$$

is linked to the total macroscopic field (ϵ_∞ is the dielectric constant for induced electronic polarization), such that the polarization (and also the total electric field strength) will vary with position and time as well as with the geometry of the system. During simulations of the electropore formation process, in particular, the membrane geometry changes drastically, thus implying considerable changes in the (total) electric field strengths.

Whereas analytic solutions for homogeneous dipole distributions are known (50), here the situation is complicated by the fact that the alternating lipid phases (low dielectric medium) and water phases (high dielectric) in the periodic simulation setup reduce the effective electric field with respect to a homogeneous system discussed above. The macroscopic fields within the water phase (thickness d_w , dielectric constant ϵ_w) and the lipid phase (d_L , ϵ_L , $d = d_w + d_L$) are given by

$$E_w = \frac{d}{d_w + d_L \frac{\epsilon_w}{\epsilon_L}} E_{\text{ext}}, \quad (4)$$

TABLE 1 Simulated lipid bilayer systems and applied electric field strengths

System	No. of lipids	Applied electric field	Simulation times
A	128 POPC	0.1–0.7 V/nm	0.3–200 ns
B	512 POPC	0.04 V/nm	50 ns

and

$$E_L = \frac{d}{d_L + d_w \frac{\epsilon_L}{\epsilon_w}} E_{\text{ext}}. \quad (5)$$

However, the dielectric constant of the lipid phase d_L in this simplified setup with two well-separated phases is unknown. Therefore, rather than aiming at an analytic treatment of the heterogeneous system at hand, we here used the average water dipole orientation within the bulk phase seen in our simulations as a probe for the effective macroscopic electric field within this phase (see also Tieleman and Berendsen (51)). We note that this problem cannot be overcome by changing the boundary conditions; whereas other boundary conditions (e.g., $\epsilon = 1$ or $\epsilon = 80$) will cause smaller artifacts, their analytic treatment for the homogeneous case is more involved. We therefore preferred to use tinfoil boundary conditions for this purpose.

Accordingly, we related the measured average bulk water dipole orientation $\langle \mu_{w,\text{eff}}(E) \rangle$ in the heterogeneous system at hand to the one predicted for a homogeneous infinite system and deduced the macroscopic electric field \mathbf{E}_w inducing the respective orientation according to Eqs. 2 and 3,

$$\langle \mu_{w,\text{eff}}(E) \rangle = \frac{1}{n_0} P, \quad (6)$$

with the number of water molecules per unit volume n_0 . In Eq. 3, the dielectric constant ϵ is field-dependent. In the Onsager-Kirkwood-Fröhlich model of dielectric polarization (52), the dielectric constant can be expressed as

$$\epsilon(E) = \epsilon_\infty + n_0 g \frac{\mu_w^2}{2k_B T} \left\{ 1 - \frac{1}{15} \left(\frac{3\mu_w E}{2k_B T} \right)^2 + \dots \right\}. \quad (7)$$

The value $\epsilon_\infty \approx 2.0$ is approximately similar to the square of the optical refractive index n , μ_w is the dipole moment of water molecules in bulk water, $g = 2.6$ is a factor measuring intermolecular correlations, and T is the absolute temperature (see also (53) for a thorough discussion of dielectric constants obtained from MD simulations). Fig. 3 shows the bulk water dipole moments $\langle \mu_{w,\text{eff}} \rangle$ from our bilayer simulations as a function of the applied external electric field and as a function of the computed macroscopic electric fields E_w (from Eq. 3) in the water phase and E_L in the lipid phase (see below). The macroscopic field for the water phase of the simulated water-bilayer system is smaller by a factor of ≈ 13 than the applied external field (note that the dielectric constant varies by $<0.2\%$ for the investigated field strengths E_w). From the total thickness of the water phase d_w and of the lipid phase d_L , we can now derive the voltage U_L across the lipid bilayer according to

$$U_L = U_{\text{tot}} - U_w, \quad (8)$$

$$= U_{\text{tot}} - d_w E_w. \quad (9)$$

$U_{\text{tot}} = E_{\text{ext}} d$ is the total voltage across the simulation box of length $d \approx 7.45$ nm normal to the membrane. Because U_L is also given by

$$U_L = \frac{d_L \epsilon_w}{\epsilon_L d_w} U_w, \quad (10)$$

Eqs. 9 and 10 enable us to determine both the voltage across the lipid bilayer and the dielectric constant ϵ_L of the membrane ($d_{L,w}$ is the lipid bilayer/water slab thickness). The macroscopic electric field E_L across the membrane is then given by

$$E_L = \frac{U_L}{d_L}. \quad (11)$$

The field E_L is larger by a factor 1.75 than the external electric field (see Fig. 3), the membrane dielectric constant varies between 2.74 and 2.75 for the field strengths investigated (with $d_L = 4.11$ nm determined from the simulations, computed as the distance between the phosphorus atoms of both monolayers).

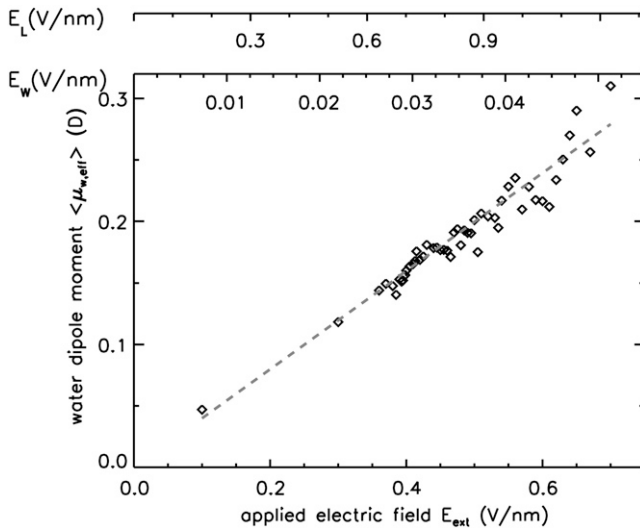


FIGURE 3 Average effective bulk water dipole moments $\langle \mu_{w,\text{eff}} \rangle$ in field direction as a function of the applied electric field E_{ext} and as a function of the macroscopic electric field in the water E_w and in the lipid phase E_L (see text). The dashed line shows the average water dipole moment according to Eq. 3 as a function of E_w . The total molecular dipole moment for the SPC water model is 2.27 D (61), from experiment a value of 2.9 ± 0.6 D was reported (62).

In summary, the effective macroscopic field is different for both bulk water phase and the lipid phase from the applied external field (similar to the experimental situation). For the study of a hydrophilic pore in equilibrium, the external field was decreased after a prepore was formed to keep the effective field in the pore region similar to the situation before the pore was formed.

Determination of the effective electric field in the experiments

In the experiments, the calculation of the voltage across membranes has to additionally consider the fact that ionic solutions are used. Accordingly, in planar lipid membrane patches, the field E across a membrane results in an average membrane field E_M (to be compared with the macroscopic field E_L determined from the simulations) of

$$E_M = \frac{E}{\epsilon_M} = \frac{U_M}{d_M}. \quad (12)$$

Here, U_M is the voltage across the membrane and ϵ_M the dielectric constant of the nonpolar lipid phase. The actual distance d_M is given by the ions charging both sides of the membrane. Cations may bind close to the hydrophobic core to the carbonyl oxygens (37,40,54) while anions form a diffusive ion layer close to the membrane surface. For simplicity, we assumed in the following that the voltage drops across the membrane thickness $d_M \approx 4.2$ nm.

The external field E_{ext} across spherical vesicles of radius r_v induces a field E_{pole} across the membrane at the vesicle pole caps of

$$E_M \approx \frac{3}{2} \frac{r_v}{d_M} E_{\text{ext}} f_\lambda, \quad (13)$$

where $f_\lambda (\leq 1)$ is the field reduction factor for conductive membranes (18). For small unilamellar vesicles of radius $r_v = 90$ nm, the ratio of the membrane field and the external field is given by $E_M/E_{\text{ext}} \approx 27$ at zero membrane conductivity ($f_\lambda = 1$). For the fast timescales considered here, it is important to take into account that the membrane field builds up according to

$$E_M(t) = E_M(1 - e^{-t/\tau_{\text{pol}}}), \quad (14)$$

where $\tau_{\text{pol}} = 80$ ns is the ionic polarization time constant of the Maxwell/Wagner polarization of these small vesicles. At $t = 80$ ns, the membrane is charged up to 64%. Since it is not known whether the polarization time constants are field-dependent, the numerical values of field strength E_M used here represent the upper limit and the calculated values for the field strengths are probably smaller than those given. As an example, the external field strength $E_{\text{ext}} = 1$ MV/m corresponds to an applied macroscopic field of strength $E = 0.027$ V/nm.

To compare the kinetics of the field-induced pore formation between experiment and simulation we determined the time delay t^* for pore formation (32). The experimental delay time τ_{delay} is given by $\tau_{\text{delay}} = \tau^* + \tau_{\text{machine}}$, where $\tau_{\text{machine}} = 0.15 \mu\text{s}$ is the machine response time (32).

Comparison of pore formation times with experiment

As already mentioned, comparison of pore formation kinetics derived from our simulations with experimental data is not straightforward. In particular, pore formation times derived from simulation, t^* , are a different observable than the kinetic time constants τ seen, e.g., in vesicle swelling assays (32), and, therefore, the obtained values cannot directly be compared.

To properly relate τ and t^* , we consider a (macroscopic) membrane patch of initial area $A(t=0) = A_0$, subjected at time $t = 0$ to a constant electric field \mathbf{E} which is oriented perpendicular to the patch. As the simplest kinetic scheme consistent with the experimental data (32), we assume the sequential reaction shown in Fig. 4. It comprises two intermediates—a tilted lipid headgroup intermediate T and a prepore intermediate Q . As suggested from

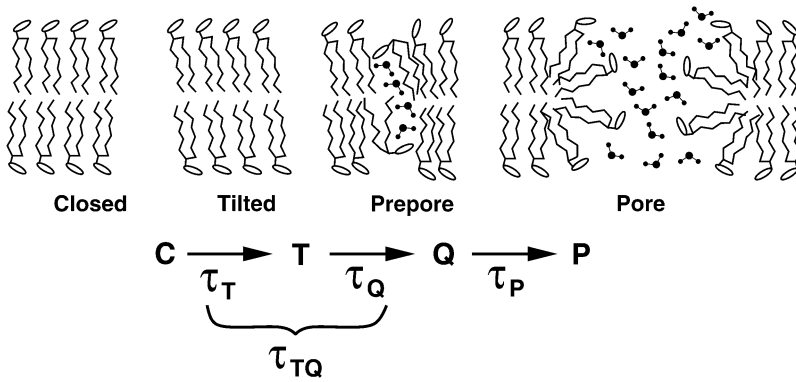


FIGURE 4 Kinetic model of pore formation. In a first step, resulting in intermediate T , the polar lipid headgroups become tilted. Tilting occurs in opposite directions for the two leaflets. In a second step, Q , one or two lipid headgroups and a few water molecules intrude into the bilayer and form a polar chain. Pore formation, P , is the last step considered in this work.

the simulations, the latter is characterized by a single membrane spanning file of 3–5 polar lipid headgroups and water molecules.

A mean prepore formation time $\langle t_{TQ} \rangle$ and a time constant τ_T for lipid tilting were extracted from each of the simulations. To determine τ_T , the average z -component of the lipid headgroup dipole was determined as a function of time. The initial part of the resulting traces ($= \min\{10 \text{ ns}, T\}$, T total simulation length) was fitted with a single exponential, yielding the rate coefficient τ_T . For $\langle t_{TQ} \rangle$, each of the 48 simulations was visually inspected and the instance of single file completion was determined manually (compare to Fig. 9). Note that, in contrast to τ_T , $\langle t_{TQ} \rangle$ is not assumed to follow from a single exponential decay, hence the different notation.

Although pore formation was observed in most of the simulations, we preferred to analyze prepore formation times over pore formation times for comparison with experiment, because after prepore formation the effective field applied in the simulations is difficult to control, or even to assess. In particular, for the PME method with external field and tinfoil boundary conditions applied here, the effective field is expected to drastically increase after formation of a high-dielectric membrane spanning bridge of water and lipid headgroups. Accordingly, pore formation is likely severely accelerated after formation of the prepore intermediate Q , which precludes direct comparison with experiment.

The probability of pore formation per unit area and unit time under the influence of an external electric field is here described by the three rate coefficients defined in Fig. 4. Each newly formed pore will 1), increase the total area of the patch, $A(t)$ (which is measured in the vesicle swelling assay) by an amount of ΔA ; and 2), decrease the area of intact membrane available for subsequent pore formation events.

Denoting the number of lipid molecules associated with the closed state by $n_C(t)$, the number of lipid molecules associated with the tilted state by $n_T(t)$, the number of prepore states (each involving possibly several lipids) by $N_Q(t)$, and the number of formed pores by $N_P(t)$, the following kinetic equations follow from Fig. 4, with rate coefficients k_T , k_Q , and k_P :

$$\dot{n}_C = -k_T n_C, \quad (15)$$

$$\dot{n}_T = k_T n_C - k_Q n_T - k_P P N_Q, \quad (16)$$

$$\dot{N}_Q = \frac{1}{Q} k_Q n_T - k_P N_Q, \quad (17)$$

$$\dot{N}_P = k_P N_Q. \quad (18)$$

Here, back-reactions are neglected. Note that n_C and n_T , respectively, count numbers of lipids, whereas N_Q and N_P count numbers of water/lipid files and pores, respectively, each involving several lipids. The numbers Q and P quantify the number of lipids that is removed from the pool of lipids available for future prepore and pore formation, respectively, by each (pre)pore formation event. In particular, for each formed pore, there are $P + Q$ less lipid molecules available for future pore formation.

From the assumed sequential scheme, and further assuming that the first two intermediates do not involve significant lipid area changes, the relative surface area increase $f(t)$ seen in the experiment follows

$$f(t) = f_0 \left[1 - x_P e^{-t/\tau_P} + x_Q e^{-t/\tau_Q} - x_T e^{-t/\tau_T} \right], \quad (19)$$

with time constants $\tau_T < \tau_Q < \tau_P$. Due to uncertainties of the fit, only τ_P and $\tau_T + \tau_Q$ could be determined reliably; for the individual τ_T and τ_Q , large uncertainties are involved in the fits to the relative increase in surface area (32). Solving the above kinetic equation for the initial conditions $n_C(t=0) = N_0$ (the number of lipid molecules in the system) and $n_T(t=0) = N_Q(t=0) = N_P(t=0) = 0$, one obtains

$$k_Q = \frac{\tau_Q + \tau_P}{2\tau_P\tau_Q} \pm \sqrt{\frac{(\tau_P + \tau_Q)^2}{4\tau_P^2\tau_Q^2} - \frac{Q}{P+Q} \frac{1}{\tau_P\tau_Q}}. \quad (20)$$

Because the tilting of the lipid bilayer headgroups involves an ensemble average for both, the experiment and the simulation (containing N_0 lipid molecules), τ_T can be directly compared to experiment.

For τ_Q and τ_P , in contrast, note that simulations enable one to observe individual pore formation events. Typically, and also in this work, each of the 48 simulations was stopped after formation of the first pore because the changed spatial distribution of the dielectric constant of the system due to pore formation would complicate the quantitative interpretation of subsequent pore formation events.

Hence, the observable that is obtained from simulation is a mean first pore formation time,

$$\langle t^* \rangle = \tau_T + \frac{1}{N_0 k_Q}, \quad (21)$$

i.e., the average time required for the first pore formation event for the N_0 lipid molecules in the simulation system. Here, on the single pore level, Q and P do not enter. Instead, and in contrast to the ensemble measurements, the mean pore formation time depends on the size N_0 of the simulation system, a fact which has not been considered in previous studies (21,23,24).

Combining Eqs. 20 and 21, the ratio P/Q has been determined from comparison of the experimental k_Q with the one obtained from simulation.

Distribution of individual pore formation times

The distribution of the pore formation times obtained from the 48 simulation runs was analyzed and compared to one-step kinetics (no intermediate) and two-step kinetic (one intermediate), respectively. Because histograms from only 48 data points suffer from large statistical errors and, hence, are difficult to compare, cumulative distributions were determined and used.

From the simulation data (see Fig. 11), the distribution of pore formation time with respect to the linear fit was determined by first subtracting the fit

function from the (logarithmic) pore formation times and subsequent accumulation.

For one-step kinetics, the pore formation times should follow an exponential distribution, $p_1(t) \propto \exp(-t/\tau_1)$, with one time constant $\tau_1 = \tau_{TQ}$. For two-step kinetics, a Poisson statistics of first order, $p_2(t) \propto t \exp(-t/\tau_2)$ is expected. For simplicity, $\tau_2 = \tau_T = \tau_Q$ was chosen such that the respective average pore formation times are identical; this choice turned out to be sufficient to explain the data. To also assess the scatter of the cumulative distributions due to the small number of 48 events, 48 pore formation times were chosen at random from the two distributions. This was done several times, and the scatter of the obtained cumulative frequencies was compared to the cumulative frequencies obtained from the simulation data.

RESULTS AND DISCUSSION

Influence of external electric fields on lipid bilayers

To investigate the effects of electric fields on lipid bilayers, lipid head dipole orientation distributions were analyzed both for the low-field simulations ($E = 0.1$ V/nm and $E = 0.3$ V/nm) and for the high-field simulations (above $E = 0.3$ V/nm) (Fig. 5). For the high-field simulations, only the part preceding pore formation of the respective trajectory was used. For the two low-field simulations, no pores were observed despite the extended simulation length of 100 ns and 200 ns, respectively.

In all simulations, the applied electric field had only a minor effect on the area per lipid (data not shown). In contrast, and as shown in Fig. 5, the average angle between the lipid dipoles and the membrane normal changed markedly, with clear differences for the two monolayers. For the monolayer of which the lipid dipoles are oriented in the direction of the applied field (cathodic leaflet), the dipoles tend to align with the field, as seen from the decreasing angle with

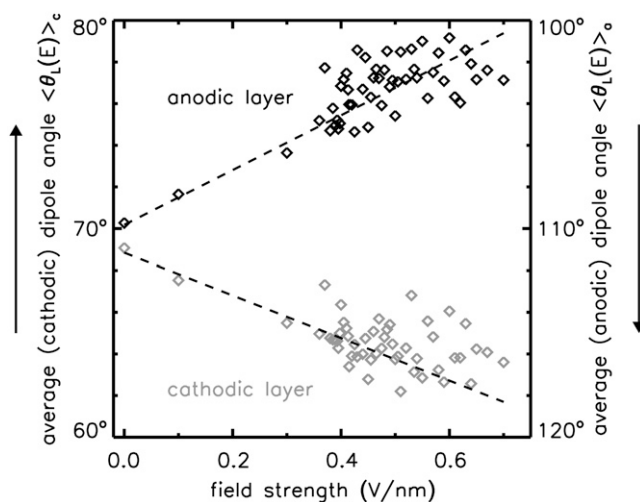


FIGURE 5 Average lipid dipole orientation. Shown are the average angles θ to the membrane normal in the direction of the applied external electric field separately for the two monolayers as a function of the applied field strength. The dashed lines show a linear fit to the data.

increasing field strength (*shaded diamonds*). For the opposite monolayer (anodic leaflet), the dipoles tend to point toward the bilayer core (*solid*). The changes in the dipole orientation at moderate to high field strengths are larger for the anodic leaflet as compared to the cathodic leaflet. It is interesting to note that this is connected to a relative increase of the lipid dipole moment in field direction of $\approx 30\%$ for the cathodic leaflet (at $E_{\text{ext}} = 0.6$ V/nm) but of $\approx 40\%$ for the anodic leaflet (see also Fig. 10).

The change in preferred lipid dipole orientation is also seen in more detail in the dipole angle probability distribution (Fig. 6), where the unperturbed (zero-field) angle distributions (*red*) are compared with those obtained for $E = 0.1, 0.3,$ and 0.393 V/nm (*yellow, green, and blue curves*). Furthermore, the distributions show that at an electric field strength of 0.393 V/nm, $\sim 35\%$ of the headgroups of the anodic leaflet (*lower panel*) enclose an angle of $< 90^\circ$ with the bilayer normal in direction of the applied external electric field (*blue line*), i.e., point toward the bilayer core, compared to only 28% for the field-free case ($\geq 90^\circ$). For the cathodic leaflet, the respective fraction is reduced by the field to 20% . Interestingly, for a small electric field (0.1 V/nm), the lipid dipole distribution for the anodic leaflet hardly changes. The field-

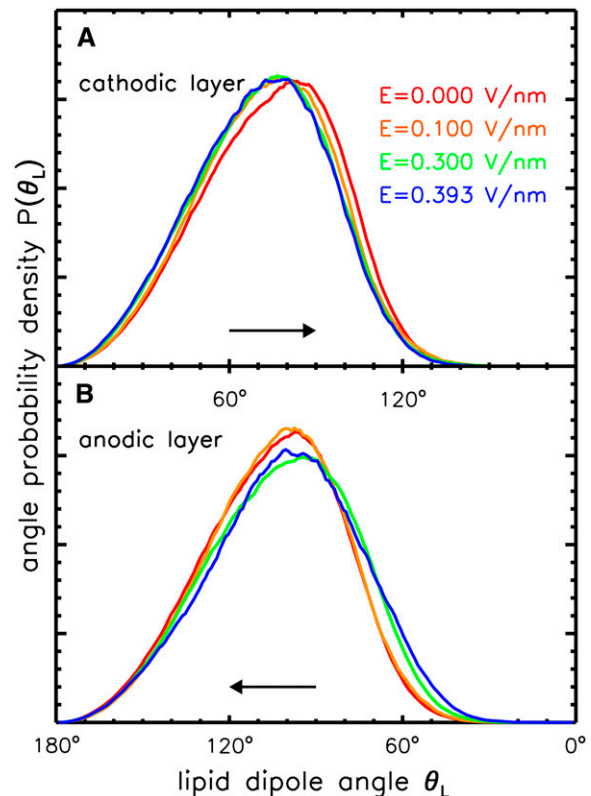


FIGURE 6 Lipid dipole angle probability density $P(\theta_L)$ as a function of the angle θ_L with respect to the membrane normal in the direction of the applied external electric field, separately for the two monolayers and for different field strengths (color-coded).

induced asymmetry in lipid dipole distribution between the two lipid leaflets implies, in turn, a tiny change in the average field-induced torque on the lipid dipoles. While the average torque is decreased for the cathodic leaflet due to lipid reorientation by 1.5% (0.3 V/nm), it is hardly changed for the anodic leaflet (+0.2%).

How and to what extent does this pronounced asymmetry between the two monolayers—in particular, the different lipid headgroup orientation—affect bilayer dynamics and possibly destabilize the membranes? It is, e.g., conceivable that lipids in the cathodic leaflet pack more closely together due to the stronger lipid dipole alignment, whereas the opposite lipids of the anodic leaflet would occupy a larger area due to the fact that more lipid dipoles are oriented perpendicular to the bilayer normal. This differential electric field effect on the lipid area would then enhance protrusions or small-scale undulations.

Fig. 7 supports this picture. Shown is the number of single-lipid protrusions (as defined in Methods) per nanosecond observed in the simulations for the above four field strengths, which fluctuate strongly (note that only the first 40 ns of the 0.393 V/nm trajectory (*blue*) were used, because subsequently pore formation started). As expected, the average numbers of single-lipid protrusions (*dashed lines*) increases from $(1.5 \pm 0.1) \text{ ns}^{-1}$ for the zero-field case to $\sim(3.9 \pm 0.4) \text{ ns}^{-1}$ for $E = 0.393 \text{ V/nm}$. No significant difference in the protrusion frequency between the anodic and the cathodic leaflets was observed. The fact that no significant difference is seen between the unperturbed simulation and the one with low field strength $E = 0.1 \text{ V/nm}$, whereas large differences occur for the higher field strengths, points toward a strongly nonlinear (e.g., exponential) behavior. Clearly, more statistics would be required to test whether the number of protrusions actually grows exponentially with field strength, which is outside the scope of this article.

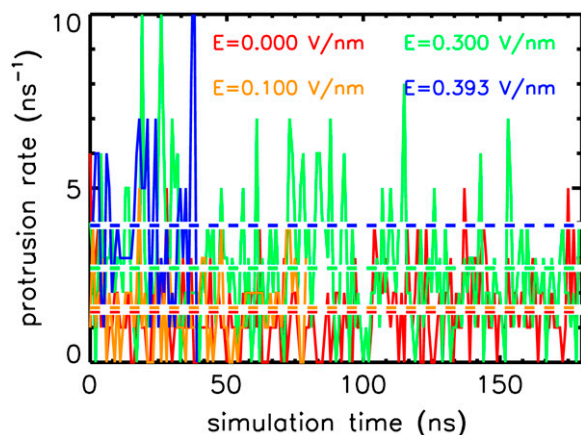


FIGURE 7 Number of protrusions (per nanosecond) for various electric field strengths. The averages are shown as dashed lines.

Influence of external electric fields on interfacial water

The asymmetry of the lipid headgroup orientation between the two monolayers induces a corresponding asymmetry in the interfacial water regions, which can be seen from the orientational distribution of water molecules in these regions. Fig. 8 shows histograms of the time-averaged water dipole orientation with respect to the membrane normal as a function of distance z from the center of the bilayer for the unperturbed case (Fig. 8 A) and for the three field strengths considered above (Fig. 8, B–D).

As can be seen, already for the zero-field case, water molecules within the hydrophilic lipid headgroup region and a few Angstroms beyond show a pronounced preference for anti-parallel dipole orientations with respect to the lipid dipoles (*orange and red* in Fig. 8). As has been shown before, this anisotropy even overcompensates for the electrostatic potential jump caused by the lipid dipoles (37), which underscores the strong influence of interfacial water on membrane electrostatics. Dipoles of the bound water molecules close to the bilayer core almost exclusively point toward the interior of the bilayer (angles 0 – 90° for the left layer, 90 – 180° for the right layer, respectively), as evidenced by the asymmetric dipole distribution close to the hydrophobic core (*blue*).

As shown in Fig. 8, B–D, the external electric field causes an additional water polarization, as clearly seen in the bulk water region for larger electric fields (Fig. 8 D). The maxi-

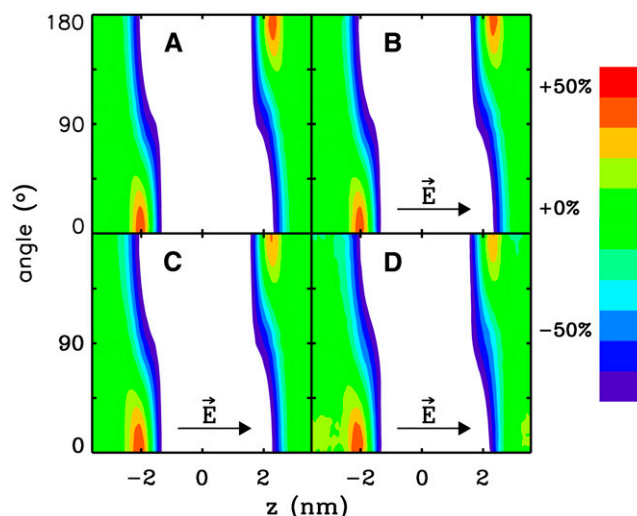


FIGURE 8 Average water molecule dipole distributions. Shown are the dipole angle (θ) distributions with respect to the z axis as a function of position across the bilayer (z) for four different simulations with different field strengths (A, $E = 0.0 \text{ V/nm}$; B, $E = 0.1 \text{ V/nm}$; C, $E = 0.3 \text{ V/nm}$; and D, $E = 0.393 \text{ V/nm}$). The distributions are weighted with $\sin(\theta)$. The color reflects the relative water density for the particular angle θ of the respective slice, e.g., in the green colored regions, the water dipoles are isotropically distributed and in the red areas, a 50% excess of the affected angles with respect to the bulk water phase is observed. In the lipid headgroup region, the water dipoles are oppositely directed to the lipid dipoles, i.e., they are pointing into the hydrophobic core.

imum of the water dipole distribution in the cathodic interfacial region ($z > 0$ nm) is decreased and increased in the anodic region ($z < 0$ nm). In summary, electric fields alter the preferential orientation of water molecules at the lipid/water interface in an asymmetric manner.

Pore formation induced by electric fields

We now focus at pore formation; a representative example for $E = 0.395$ V/nm is shown in Fig. 9. For this relatively weak field strength, it took 18.7 ns in this particular case for pore formation to start. Once started, pore formation proceeded quickly within 0.5 ns, as to be expected for an activated process. In the snapshots, the lipids are shown in shading (hydrophobic tails as sticks, hydrophilic heads as spheres). Two selected lipids, which are involved in the primary steps of pore formation, are highlighted in orange; their lipid head dipoles are indicated by the colored nitrogen (*blue*) and phosphate atoms (*magenta*). Also highlighted in yellow are water molecules that participate in this primary event.

As also in all other simulations, pore formation starts with protrusions from the opposing monolayers into the membrane interior. Within such protrusions, lipids protruding from the anodic monolayer (here, lower layer) tend to change their lipid dipole orientation, thereby strongly perturbing the orientation of its fatty acyl chains. This perturbation, together with the fact that the hydrophilic headgroups of the protruding lipids drag their water shell toward the membrane interior, causes subsequent thinning of the hydrophobic bilayer core. This creates an enhanced probability for the formation of a membrane-spanning water file (at $\Delta t = 0.1$ ns, water molecules in *yellow*), which in turn drives the lipid headgroup further toward the hydrophobic core. We em-

phasize that each of the 48 observed pore formation events is preceded by the occurrence of such membrane spanning water files, which we therefore denote as a prepore formation intermediate. Although we cannot rule out occasional water files that do not induce pore formation, generally, this seems to be the “event of no return,” and pore formation always starts immediately after occurrence of the water file. As the protruding polar lipid groups drag further water molecules, a dielectric avalanche involving several dozens of water molecules starts, thereby forming the pore. We note that the latter steps after the formation of the prepore are drastically enhanced due to a changing effective macroscopic field implied by the change in system geometry (see Methods). Apparently, the probability for the triggering water file is enhanced if two protrusions from opposing leaflets form simultaneously face-to-face, and, indeed, this situation is often seen in our simulation before pore formation.

Bilayer electrostatics

To understand the forces that drag water molecules and polar lipid headgroups toward the hydrophobic bilayer core, we have analyzed the electric potential and the electric field across the bilayer as well as the resulting forces on these dipoles, as shown in Fig. 10 for the unperturbed case (*black*) and for $E = 0.1$ V/nm (*blue*) and $E = 0.3$ V/nm (*red*), respectively. Note that the shown forces refer to the preferred dipole orientation, as discussed above.

As must be expected, the drop of the potential $U(z)$ caused by the external field (Fig. 10 A) occurs mainly within the low-dielectric membrane core. The electric field in direction of the bilayer normal, $E_z = -\partial_z U$, thus varies in this region between simulations with different external electric fields, too (B). It is

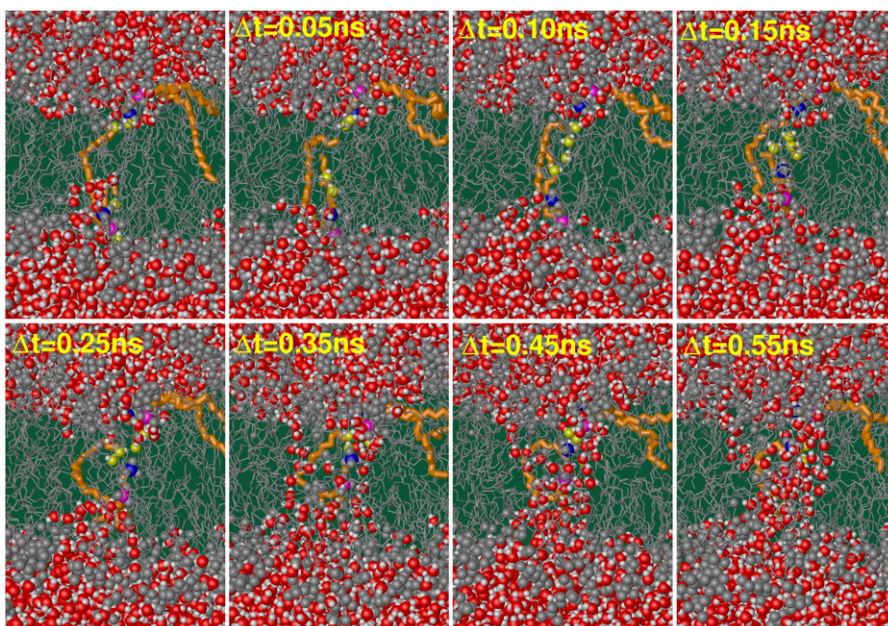


FIGURE 9 Primary electroporation events. Shown are snapshots of the electropore formation at $E = 0.395$ V/nm (after 18.7 ns). Lipids and water molecules guiding the initial steps are highlighted, the lipid headgroups are shown as gray balls, water oxygens as red balls, and lipid tails as sticks. Water molecules forming the initial membrane-spanning water file are colored yellow.

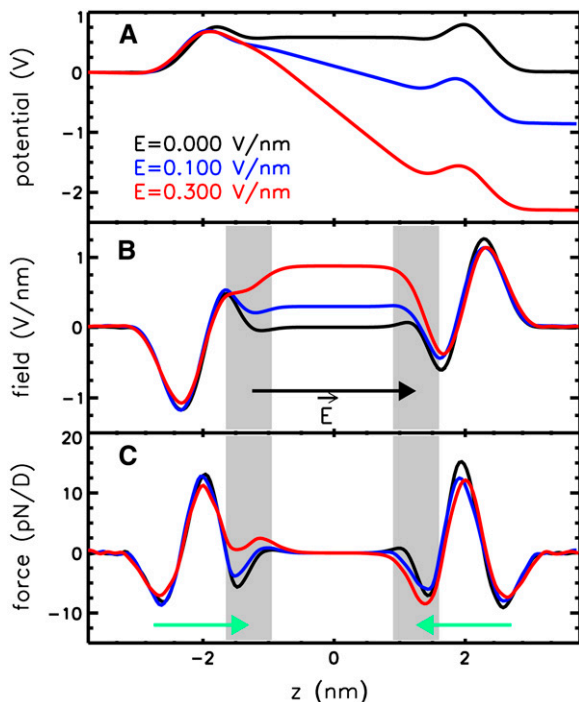


FIGURE 10 Electrostatic potential (A), field strength (B), and force on a dipole of strength 1 D (1 Debye = $3.33564 \cdot 10^{-30}$ Cm) (C) across the lipid bilayer for three different field strengths. The region imposing asymmetry among the two monolayers is shaded. The direction of the external applied electric field is given by a solid arrow (B), the average water dipole direction by green arrows (C). The electric field strengths were obtained by integration of the averaged charge density across the bilayer, after summing the charges per slice (box divided in 200 slices), the electrostatic potential was computed by double integration of the charge density. The force on a dipole was obtained by numerical differentiation of the electric field strength. The force was smoothed with a Gaussian with a width of 0.08 nm.

positive, exhibiting an asymmetry between the two leaflets in the transition region between hydrophilic headgroups and fatty acyl chains (*shaded*). A bump appears on the side of the anodic monolayer (at ~ 2.5 nm) which is due to the (differential) shift of the lipid dipole angles of this layer toward values $>90^\circ$ (see Fig. 6).

As seen in Fig. 10 C, the force F (given in pN/D) acting on the dipole of a water molecule increases in the interfacial anodic region with increasing field strength, whereas it decreases at the opposite interfacial cathodic region. For sufficiently strong electric fields (>0.2 V/nm), the force in the interfacial anodic region changes direction (*red line*) and thus pulls water molecules with a dipole orientation in direction of the external field (*green arrows* in Fig. 10 C, compare Fig. 8) into the hydrophobic core. In the interfacial cathodic region, in contrast, the forces on water dipoles act toward the headgroups. Therefore, the poration process preferably starts with water molecules protruding the lipid bilayer from the anodic monolayer toward the bilayer core. Interestingly, for asymmetric bilayers with a PS in the cathodic leaflet, pore formation preferentially starts from the cathodic leaflet (30).

The depicted forces also show why water molecules usually do not enter the bilayer core in the absence of an external electric field. A force well in the interfacial region of both leaflets attracts the water dipoles in direction of the headgroups and thereby confines them.

Analysis of prepore formation times

Pore formation has been observed in 48 simulations with electric field strengths ranging from 0.36–0.70 V/nm. Fig. 11 A shows the (logarithmic) pore formation times t^* (*shaded*), determined as the time span between onset of the electric field and observation of the first closed water/lipid file across the membrane core (state Q). The solid data points were derived from the measured swelling kinetics as described in Methods. Assuming one main activation barrier, the distribution of pore formation times can be described by the Ansatz,

$$t^* = t_0^* e^{-\frac{\int \langle \Delta \mu \rangle dE}{k_B T}}, \quad (22)$$

with the change in the average activation dipole moment $\langle \mu \rangle$ upon the pore formation event. The pore formation times obtained both from experiment and from the simulations follow a simple exponential (*dashed line*),

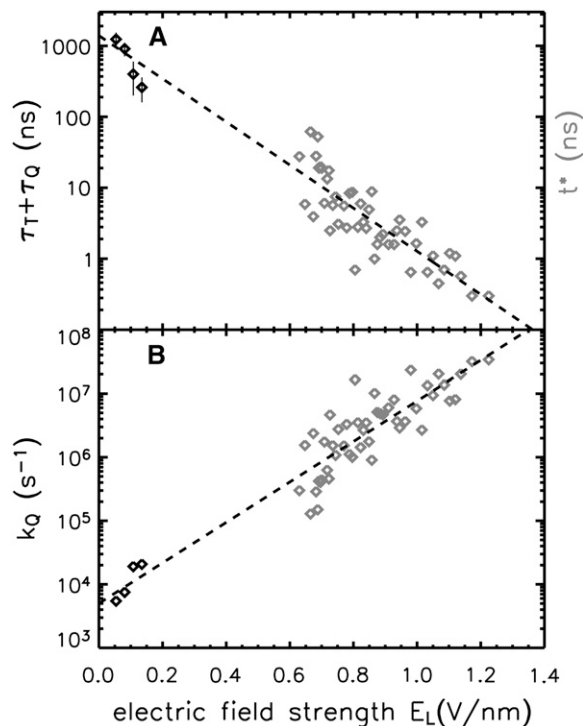


FIGURE 11 Preparation time t^* (simulation, *shaded symbols*) and experimental time constant $\tau_T + \tau_Q$ (*solid symbols*, A), and pore formation rate coefficient k_Q (B) as a function of the effective macroscopic electric field E_L across the lipid bilayer. Data from experiment are shown in solid representation (32). The dashed line is a fit to the simulation data according to $t^* \sim \exp(-\Delta \mu E_L)$.

$$t^* \sim e^{\frac{\Delta\mu E_L}{k_B T}}, \quad (23)$$

with a scatter of expected size (see below), i.e., $\langle \Delta\mu \rangle$ can be treated as being independent of the field strength E_L . From the fit to the data, a change in dipole moment in direction of the external field of $\langle \Delta\mu \rangle \approx 30 \cdot 10^{-30}$ Cm was obtained. Thus pore formation is accompanied by a change in dipole moment of only $\sim 9 D$. With this single fit parameter, excellent agreement with experiment is seen (Fig. 11). Furthermore, the data rule out a quadratic dependence of the activation energy for prepore formation on the electric field, as has been proposed for the pore formation process (55). Note that the effective field \mathbf{E}_F , which determines the torque $\boldsymbol{\mu} \times \mathbf{E}_F$ on a dipole $\boldsymbol{\mu}$, usually differs from \mathbf{E}_L by a factor $\alpha < 1$, as described by the Fröhlich theory: For hydrated spheroidal dipoles, the Fröhlich field is $E_F = (\epsilon_{hs})/(\epsilon_{hs} + (\epsilon_\infty - \epsilon_{hs})A_\alpha)E_{hs}$, with $E_{hs} = (\epsilon_W/\epsilon_{hs})E_W$ the field strength within the hydration shell (52). Using the hydrated lipid headgroup values $A_\alpha = 0.14$, $\epsilon_{hs} = 5$, and $\epsilon_\infty = 2.0$ (52,56), one obtains as a simple estimate $E_F \approx 0.5E_L$. Thus, $\langle \Delta\mu \rangle$ is a lower bound for the activation dipole moment.

Fig. 11 *B* shows the prepore formation rate coefficient k_Q both for the simulation data and for the experiment. From Eqs. 20 and 21, a ratio of the numbers of lipids involved in prepore (Q) and pore (P) formation, $P/Q \approx 35$, is obtained; hence, inserting $Q \approx 4$ (estimated from prepore intermediates observed in the simulations) yields $P \approx 140$, i.e., each pore removes ~ 140 lipids from the pool of all lipids available for subsequent pores. Thus, for the chosen simulation system with 128 lipids one would expect not more than one pore to form. From this result one would predict that pores are separated typically by ~ 7 nm.

Distribution of individual pore formation times

To describe the measured membrane area kinetics (32), three exponentials have been found to be necessary, which implies (at least) one intermediate between the closed state C and the prepore state Q .

From visual inspection of the pore formation simulations, however, no such intermediate could be identified, which

raises the question if such an intermediate actually exists in the simulations. To address this question, we compared the (cumulative) distribution of pore formation times (normalized by the linear fit which describes the field dependence, *dashed line* in Fig. 11) to the distributions (*bold lines*) expected for a one-step process (Fig. 12, *left*) and that expected for a two-step process (*right*). For both kinetics, 20 samples of 48 each were drawn from the respective distribution functions (see Methods) and plotted as an ensemble of cumulative distribution functions (*thin lines*), thus quantifying the scatter of distribution functions expected for the small (48) number of pore formation times.

As can be seen, the distribution obtained from the pore formation simulations differs significantly from the distributions expected for a one-step kinetics with no intermediates (*left*). Clearly, parts of the distribution lie outside the ensemble drawn from a one-step process. In contrast, a two-step process (*right*) apparently describes the simulation data perfectly well. From this, we conclude that also in the simulations an intermediate occurs, which we identify with the intermediate with tilted lipid headgroups described above. The simulation agrees with the available experimental data in that it predicts the same reaction scheme. Values for the time constant τ_T for lipid tilting determined from the simulations (see Methods) range between 0.1 ns (large field strengths) and 5 ns (low field strengths). Experimentally, this time constant can be estimated from a fit to the surface increase of vesicles due to electropore formation. In line with the simulation results, τ_T increases for smaller electric field strengths. It varies between 0.7 μ s and 0.1 μ s for electric membrane fields between 0.054 V/nm and 0.135 V/nm (these values are subject to large error bars, estimated to 50%).

Characteristics of a stable electropore

The equilibrium properties of an electropore were studied for a larger bilayer system with 512 POPC molecules. A pore intermediate was formed first at a high external field strength of 0.5 V/nm. Subsequently, the simulation was continued at a decreased field strength of 0.04 V/nm to avoid artificially increased effective electric fields in the pore region due to

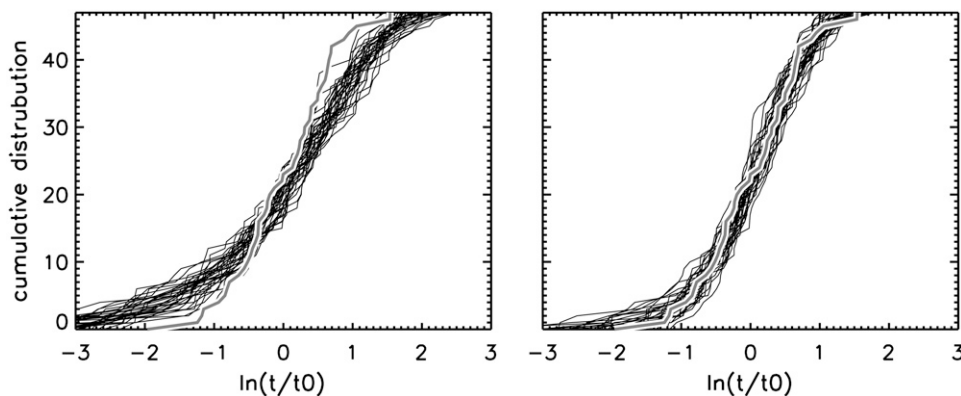


FIGURE 12 E-field-normalized cumulative distribution functions (*thick shaded lines*, logarithmic timescale) obtained from the 48 individual pore formation times observed in the molecular dynamics simulations. (*Left*) Superimposed are 25 cumulative distribution functions for 48 events each, drawn from an exponential distribution, corresponding to a one-step kinetics with no intermediates. (*Right*) Here, the 25 cumulative distributions were drawn from two-step kinetics, i.e., assuming one intermediate.

artifacts introduced by the periodic boundary conditions (see Methods). The decreased external field strength was chosen such as to keep the effective macroscopic electric fields in the pore region stable. It has to be noted, however, that the electric field strength across intact parts of the lipid bilayer is significantly lowered with respect to the initial pore-inducing electric field.

The number of lipids aligning the hydrophilic pore (compare Fig. 2) equilibrates within 20 ns to ~ 8 (10) (number of lipids with phosphate group within 0.7 (0.9) nm from the bilayer center). The average number of water molecules within these regions of the pore is 57 (75), comparable to pores induced by charge imbalance across the membrane (27). The effective pore area is estimated to only 0.7 ± 0.4 nm² from the difference of the total area between the bilayer patch containing the pore and a control simulation (50 ns without electric field, data not shown). The corresponding pore radius of 0.47 ± 0.15 nm is in good agreement with the mean pore radius derived from conductivity measurements on planar lipid membranes (5 Å) (57) or electrooptical experiments (0.35 ± 0.05 nm) (34,32).

SUMMARY AND CONCLUSIONS

Despite a number of experimental and theoretical studies, the detailed mechanism underlying electropore formation has so far been unresolved. Experiments led to the concept of an intermediate hydrophobic pore during the transition to hydrophilic pores (16,58) or even require to assume a second intermediate (32). Here we provided atomic insight by molecular dynamics simulations of the poration process. Electropore formation was found to be accelerated by asymmetrical changes in the preferred dipole orientations between the two monolayers of both lipids and water molecules in the presence of external electric fields across the membrane, resulting in asymmetrical electric fields especially in the transition region between the hydrophobic core and the hydrophilic headgroup region (see also Tieleman (21)). Probably coupled to this asymmetry, the number of lipid protrusions increased significantly. This finding is supported by previous simulation studies reporting increased electric field strengths required for pore formation for an octane slab (21) or a POPC bilayer with all partial atomic charges set to zero (22). As also reported earlier (21), field gradients at the interface lipid headgroup/hydrophobic core were seen to effectively decrease the free energy barrier for pore formation. Different from the case of asymmetric PS/PC membranes (30), pore formation preferentially started at the anodic leaflet.

However, previous simulations did not provide intermediate states and equilibrium pore sizes. Here, by analysis of 48 poration simulations performed for different electric field strengths, simulation results could be reconciled with experimental findings. In particular, by analyses of the distribution of prepore formation times and comparison to kinetic

experiments, we suggest two intermediates: a state with modified headgroup orientation (T), depending on the strength of the external field; and a prepore state (Q) with a closed water-lipid file across the membrane (Fig. 4). Such a defect was described before as the initial step of pore formation (21,27). The prepore intermediate is likely to be nonconductive and thus may be identified as the intermediate found in conductance measurements on planar lipid bilayers (17). Further, an analysis of the effective electric fields acting across lipid bilayers in typical simulation setups enabled the study of the equilibrium properties of a stable hydrophilic pore. In agreement with experiment, a pore radius of 0.5 nm was determined, with ~ 10 lipid headgroups tilting into the hydrophobic core forming a hydrophilic pore. Previously observed growing pores (10 nm radius within few nanoseconds) when applying external electric fields in periodic boundary simulations using PME (21) are potentially caused by artificially enhanced electric fields in the pore region. This view is supported by a recent study of pore formation induced by imbalanced ion concentrations on both sides of the membrane (25) where such artifacts have been avoided. Pore sizes in this non-equilibrium study were similar to the ones observed here.

In a recent study based on poration experiments at low applied voltages (17), the logarithmic creation times for single membrane pores, the pore formation times, were assumed to show a quadratic dependence on the voltage (55). In the absence of electric fields, Wohlert et al. found a quadratic dependency of the free energy of a pore for radii < 0.3 nm and a linear behavior above (59). Here, we investigated the distribution of prepore formation times both on experimental and simulation timescales. The formation of a single prepore can be described by a single exponential, the activation energy ΔG^\ddagger being linear to the applied effective electric field across the membrane. The simulation data together with the experimental data rule out a purely quadratic dependency of ΔG^\ddagger on the transmembrane voltage, as would be expected from mere consideration of the change in the pore's capacitance (see Weaver and Chizmadzhev for a thorough review on the theory of electroporation (18)).

This work involves the first direct comparison of electropore formation between experiment and molecular dynamics simulation. The statistical theory presented here shows that straightforward comparison between experimental time constants of pore formation, being ensemble averages, cannot directly be carried out with the times observed in simulations for the formation of the first pore, as these relate to single events. This can be seen by noting that, whereas the former average is independent of the membrane area observed, the latter time decreases with increasing area of the simulated membrane patch. Our theory provides the appropriate rescaling, which, in addition enables us to extract the effective number of ≈ 140 lipid molecules involved in the formation and surrounding of one aqueous electropore.

To conclude, and considering the possible importance of electroporation in electrofusion or in the treatment of skin

cancer and the associated problems, e.g., with heating of neighbored tissue upon application of external electric fields, extensive further studies using different lipid compositions, lipid-protein systems (29), or different pulse forms (60) remain necessary.

We thank Peter Tieleman for providing his modified GROMACS code which implements external electric fields before its official release, and Volker Knecht for valuable discussions. Computer time was provided by the Göttingen computer center, Gesellschaft für wissenschaftliche Datenverarbeitung, Göttingen.

Financial support by the Deutsche Forschungsgemeinschaft (Graduate School Structure Formation and Transport in Complex Systems, No. 1276/1) is acknowledged (to R.A.B.). As member of the Center for Bioinformatics, Rainer A. Böckmann is supported by the Deutsche Forschungsgemeinschaft grant No. BIZ 4/1.

REFERENCES

- Neumann, E., M. Schaefer-Ridder, Y. Wang, and P. H. Hofschneider. 1982. Gene transfer into mouse lymphoma cells by electroporation and electroporative delivery of drugs and genes. *EMBO J.* 1:841–845.
- Sale, A. J. H., and W. A. Hamilton. 1967. Effects of high electric fields on microorganisms. I. Killing of bacteria and yeast. *Biochim. Biophys. Acta.* 148:781–788.
- Neumann, E., and K. Rosenheck. 1972. Permeability changes induced by electric impulses in vesicular membranes. *J. Mol. Biol.* 10:279–290.
- Behrader, M., C. Domenge, B. Luboinski, S. Orlowski, J. Behrader, and L. M. Mir. 1993. Electrochemotherapy, a new antitumor treatment. First clinical phase I–II trial. *Cancer.* 72:3694–3700.
- Mir, L. M., S. Orlowski, J. Behrader, J. Teissie, M. P. Rols, G. Sersa, D. Miklavcic, R. Gilbert, and R. Heller. 1995. Biomedical applications of electric pulses with special emphasis on antitumor electrochemotherapy. *Bioelectrochem. Bioenerg.* 38:203–207.
- Mir, L. M., M. F. Bureau, J. Gehl, R. Rangara, D. Rouy, J.-M. Caillaud, P. Delaere, D. Branellec, B. Schwartz, and D. Scherman. 1999. High-efficiency gene transfer into skeletal muscle mediated by electric pulses. *Proc. Natl. Acad. Sci. USA.* 96:4262–4267.
- Glasspool-Malone, J., S. Somiari, J. J. Drabick, and R. W. Malone. 2000. Efficient nonviral cutaneous transfection. *Mol. Ther.* 2:140–146.
- Drabick, J. J., J. Glasspool-Malone, S. Somiari, A. King, and R. W. Malone. 2001. Cutaneous transfection and immune responses to intradermal nucleic acid vaccination are significantly enhanced by *in vivo* electroporation. *Mol. Ther.* 3:249–255.
- Saebø-Larssen, S., E. Fosberg, and G. Gaudernack. 2002. mRNA-based electrotransfection of human dendritic cells and induction of cytotoxic T lymphocyte responses against the telomerase catalytic subunit (hTERT). *J. Immunol. Methods.* 259:191–203.
- Van Meirvenne, S., L. Straetman, C. Heirman, M. Dullaers, C. De Greef, V. Van Tendeloo, and K. Thielemans. 2002. Efficient genetic modification of murine dendritic cells by electroporation with mRNA. *Cancer Gene Ther.* 9:787–797.
- Senda, M., J. Takeda, S. Abe, and T. Nakamura. 1979. Induction of cell fusion of plant protoplasts by electrical stimulation. *Plant Cell Physiol.* 20:1441–1443.
- Neumann, E., G. Gerisch, and K. Opatz. 1980. Cell fusion induced by electric impulses applied to *Dictyostelium*. *Naturwissenschaften.* 67:414–415.
- Mouneimne, Y., P. F. Tosi, Y. Gazitt, and C. Nicolau. 1989. Electroinsertion of xeno-glycophorin into the red blood-cell membrane. *Biochem. Biophys. Res. Commun.* 159:34–40.
- Chernomordik, L. V., S. I. Sukharev, S. V. Popov, V. F. Pastushenko, A. V. Sokirko, I. G. Abidor, and Y. A. Chizmadzhev. 1987. The electrical breakdown of cell and lipid membranes: the similarity of phenomenologies. *Biochim. Biophys. Acta.* 902:360–373.
- Kinosita, K., Jr., and T. Y. Tsong. 1979. Voltage-induced conductance in human erythrocyte membranes. *Biochim. Biophys. Acta.* 554:479–497.
- Abidor, I. G., V. B. Arakelyan, L. V. Chernomordik, Y. A. Chizmadzhev, V. F. Pastushenko, and M. R. Tarasevich. 1979. Electrical breakdown of bilayer lipid membranes. I. The main experimental facts and their qualitative discussion. *Bioelectrochem. Bioenerg.* 6:37–52.
- Melikov, K. C., V. A. Frolov, A. Shcherbakov, A. V. Samsonov, Y. A. Chizmadzhev, and L. V. Chernomordik. 2001. Voltage-induced non-conductive pre-pores and metastable single pores in unmodified planar lipid bilayer. *Biophys. J.* 80:1829–1836.
- Weaver, J. C., and Y. A. Chizmadzhev. 1996. Theory of electroporation: a review. *Bioelectrochem. Bioenerg.* 41:135–160.
- Kakorin, S., E. Redeker, and E. Neumann. 1998. Electroporative deformation of salt filled lipid vesicles. *Eur. Biophys. J.* 27:43–53.
- Teissie, J., and T. Y. Tsong. 1981. Electric field induced transient pores in phospholipid bilayer vesicles. *Biochemistry.* 20:1548–1554.
- Tieleman, D. P. 2004. The molecular basis of electroporation. *BMC Biochem.* 5:10.
- Vernier, P. T., and M. J. Ziegler. 2007. Nanosecond field alignment of headgroup and water dipoles in electroporating phospholipid bilayers. *J. Phys. Chem. B.* 111:12993–12996.
- Hu, Q., S. Viswanadham, R. P. Joshi, K. H. Schoenbach, S. J. Beebe, and P. F. Blackmore. 2005. Simulations of transient membrane behavior in cells subjected to a high-intensity ultrashort electric pulse. *Phys. Rev. E Stat. Nonlin. Soft Matter Phys.* 71:031914.
- Hu, Q., R. P. Joshi, and K. H. Schoenbach. 2005. Simulations of nanopore formation and phosphatidylserine externalization in lipid membranes subjected to a high-intensity, ultrashort electric pulse. *Phys. Rev. E Stat. Nonlin. Soft Matter Phys.* 72:031902.
- Gurtovenko, A. A., and I. Vattulainen. 2005. Pore formation coupled to ion transport through lipid membranes as induced by transmembrane ionic charge imbalance: atomistic molecular dynamics study. *J. Am. Chem. Soc.* 127:17570–17571.
- Gurtovenko, A. A., and I. Vattulainen. 2007. Molecular mechanism for lipid-flip-flops. *J. Phys. Chem. B.* 111:13554–13559.
- Gurtovenko, A. A., and I. Vattulainen. 2007. Ion leakage through transient water pores in protein-free lipid membranes driven by transmembrane ionic charge imbalance. *Biophys. J.* 92:1878–1890.
- Troiano, G. C., K. J. Stebe, R. M. Raphael, and L. Tung. 1999. The effects of gramicidin on electroporation of lipid bilayers. *Biophys. J.* 76:3150–3157.
- Siu, S. W. I., and R. A. Böckmann. 2007. Electric field effects on membranes: gramicidin A as a test ground. *J. Struct. Biol.* 157:545–556.
- Vernier, P. T., M. J. Ziegler, Y. Sun, W. V. Chang, M. A. Gundersen, and D. P. Tieleman. 2006. Nanopore formation and phosphatidylserine externalization in a phospholipid bilayer at high transmembrane potential. *J. Am. Chem. Soc.* 128:6288–6289.
- Pliquett, U., R. P. Joshi, V. Sridhara, and K. H. Schoenbach. 2007. High electric field effects on cell membranes. *Bioelectrochemistry.* 70:275–282.
- Griese, T., S. Kakorin, and E. Neumann. 2002. Conductometric and electrooptic relaxation spectrometry of lipid vesicle electroporation at high fields. *Phys. Chem. Chem. Phys.* 4:1217–1227.
- Chizmadzhev, Y. A., J. Teissie, and D. Walz. 2004. *Lipid Bilayer Electroporation*. Birkhäuser Verlag, Basel, Boston, Berlin.
- Kakorin, S., S. P. Stoylov, and E. Neumann. 1996. Electro-optics of membrane electroporation in diphenylhexatriene-doped lipid bilayer vesicles. *Biophys. Chem.* 58:109–116.
- Tieleman, D. P., H. Leontiadou, A. E. Mark, and S.-J. Marrink. 2003. Simulation of pore formation in lipid bilayers by mechanical stress and electric fields. *J. Am. Chem. Soc.* 125:6382–6383.
- Tarek, M. 2005. Membrane electroporation: a molecular dynamics simulation. *Biophys. J.* 88:4045–4053.

37. Böckmann, R. A., A. Hac, T. Heimburg, and H. Grubmüller. 2003. Effect of sodium chloride on a lipid bilayer. *Biophys. J.* 85:1647–1655.
38. Berger, O., O. Edholm, and F. Jähnig. 1997. Molecular dynamics simulations of a fluid bilayer of dipalmitoylphosphatidylcholine at full hydration, constant pressure, and constant temperature. *Biophys. J.* 72:2002–2013.
39. Berendsen, H. J. C., J. P. M. Postma, W. F. Van Gunsteren, and J. Hermans. 1981. Interaction Model for Water in Relation to Protein Hydration. D. Reidel, Dordrecht, The Netherlands.
40. Böckmann, R. A., and H. Grubmüller. 2004. Multistep binding of divalent cations to phospholipid bilayers: a molecular dynamics study. *Angew. Chem. Int. Ed. Engl.* 43:1021–1024.
41. Berendsen, H. J. C., D. van der Spoel, and R. van Drunen. 1995. GROMACS: a message-passing parallel molecular dynamics implementation. *Comput. Phys. Commun.* 91:43–56.
42. Lindahl, E., B. Hess, and D. van der Spoel. 2001. GROMACS 3.0: a package for molecular simulation and trajectory analysis. *J. Mol. Model.* 7:306–317.
43. Hess, B., H. Bekker, H. J. C. Berendsen, and J. G. E. M. Fraaije. 1997. LINCS: a linear constraint solver for molecular simulations. *J. Comput. Chem.* 18:1463–1472.
44. Miyamoto, S., and P. A. Kollman. 1992. SETTLE—an analytical version of the SHAKE and RATTLE algorithm for rigid water models. *J. Comput. Chem.* 13:952–962.
45. Darden, T., D. York, and L. Pedersen. 1993. Particle mesh Ewald—an N -log(N) method for Ewald sums in large systems. *J. Chem. Phys.* 98:10089–10092.
46. Leeuw, S. W., J. W. Perram, and E. R. Smith. 1986. Computer simulation of the static dielectric constant of systems with permanent electric dipoles. *Annu. Rev. Phys. Chem.* 37:245–270.
47. Leeuw, S. W., B. Smit, and C. P. Williams. 1990. Molecular studies of polar/nonpolar fluid mixtures. I. Mixtures of Lennard-Jones and Stockmayer fluids. *J. Chem. Phys.* 93:2704–2714.
48. Berendsen, H. J. C., J. P. M. Postma, W. F. van Gunsteren, A. D. Nola, and J. R. Haak. 1984. Molecular dynamics with coupling to an external bath. *J. Chem. Phys.* 81:3684–3690.
49. Neumann, M. 1983. Dipole moment fluctuation formulas in computer simulations of polar systems. *Mol. Phys.* 50:841–858.
50. Booth, F. 1951. The dielectric constant of water and the saturation effect. *J. Chem. Phys.* 19:391–394.
51. Tieleman, D. P., and H. J. C. Berendsen. 1998. A molecular dynamics study of the pores formed by *E. coli* OmpF porin in a fully hydrated palmitoylcholine bilayer. *Biophys. J.* 74:2786–2801.
52. Böttcher, C. J. F. 1973. Theory of Dielectric Polarization. Oxford University Press, London.
53. Yeh, I.-C., and M. L. Berkowitz. 1999. Dielectric constant of water at high electric fields: molecular dynamics study. *J. Chem. Phys.* 110:7935–7942.
54. Pandit, S. A., D. Bostick, and M. L. Berkowitz. 2003. Molecular dynamics simulation of a dipalmitoylphosphatidylcholine bilayer with NaCl. *Biophys. J.* 84:3743–3750.
55. Vasilkoski, Z., A. T. Esser, T. R. Gowrishankar, and J. C. Weaver. 2006. Membrane electroporation: the absolute rate equation and nanosecond time scale pore creation. *Phys. Rev. E Stat. Nonlin. Soft Matter Phys.* 74:021904.
56. Kittel, C. 1986. Introduction to Solid State Physics. Wiley, New York.
57. Glaser, R. W., S. L. Leikin, L. V. Chernomordik, V. F. Pastushenko, and A. I. Sokirko. 1988. Reversible electrical breakdown of lipid bilayers: formation and evolution of pores. *Biochim. Biophys. Acta.* 940:275–287.
58. Neumann, E., S. Kakorin, and K. Toensing. 1998. Membrane electroporation and electromechanical deformation of vesicles and cells. *Faraday Discuss.* 111:111–125.
59. Wohrlert, J., W. K. den Otter, O. Edholm, and W. J. Briels. 2006. Free energy of a trans-membrane pore calculated from atomistic molecular dynamics simulations. *J. Chem. Phys.* 124:154905.
60. Lucas, M. L., M. J. Jaroszeski, R. Gilbert, and R. Heller. 2001. In vivo electroporation using an exponentially enhanced pulse: a new waveform. *DNA Cell Biol.* 20:183–188.
61. Kiyohara, K., K. E. Gubbins, and A. Z. Panagiotopoulos. 1998. Phase coexistence properties of polarizable water models. *Mol. Phys.* 94:803–808.
62. Badyal, Y. S., M. L. Saboungi, D. L. Price, S. D. Shastri, D. R. Haefner, and A. K. Soper. 2000. Electron distribution in water. *J. Chem. Phys.* 112:9206–9208.